



Contents lists available at ScienceDirect

# International Journal of Plasticity

journal homepage: [www.elsevier.com/locate/ijplas](http://www.elsevier.com/locate/ijplas)



## Discontinuous coarsening leads to unchanged tensile properties in high-entropy alloys with different recrystallization volume fractions



Zhongsheng Yang<sup>a</sup>, Xin Liu<sup>a</sup>, Jiajun Zhao<sup>a</sup>, Qionghuan Zeng<sup>a</sup>, Kengfeng Xu<sup>a</sup>, Yue Li<sup>a</sup>, Chuanyun Wang<sup>a</sup>, Lei Wang<sup>a</sup>, Junjie Li<sup>a</sup>, Jincheng Wang<sup>a</sup>, Hyoung Seop Kim<sup>d,e,f</sup>, Zhijun Wang<sup>a,\*</sup>, Feng He<sup>a,b,c,\*</sup>

<sup>a</sup> State Key Laboratory of Solidification Processing, Northwestern Polytechnical University, Xi'an 710072, PR China

<sup>b</sup> Research & Development Institute of Northwestern Polytechnical University in Shenzhen, Shenzhen, PR China

<sup>c</sup> Collaborative Innovation Center of Northwestern Polytechnical University, Shanghai, PR China

<sup>d</sup> Graduate Institute of Ferrous & Energy Materials Technology, Pohang University of Science and Technology (POSTECH), Pohang, 37673, South Korea

<sup>e</sup> Advanced Institute for Materials Research (WPI-AIMR), Tohoku University, Sendai 980-8577, Japan

<sup>f</sup> Institute for Convergence Research and Education in Advanced Technology, Yonsei University, Seoul, 03722, South Korea

### ARTICLE INFO

#### Keywords:

High-entropy alloys

Ductility

Deformation mechanism

Discontinuous coarsening

### ABSTRACT

Heterogeneous microstructure alloys provide a possibility for the combination of strength and ductility. As a typical heterogeneous microstructure, partially recrystallized microstructure is attractive because of the convenient processing route and great potential for industrial applications. However, the mechanical properties of this microstructure vary dramatically with different morphology factors, especially the recrystallization fraction, which restricts the processing window and the property consistency. In this study, we found that the yield strength (~1.3 GPa) and ductility (~20 %) of the partially recrystallized Ni<sub>2</sub>CoCrFeTi<sub>0.24</sub>Al<sub>0.2</sub> do not change when the recrystallization fraction increases from 21 % to 72 %. This novel phenomenon is attributed to an additional hetero-deformation induced (HDI) strain hardening effect produced by heterogeneous precipitates. With the increased recrystallization fraction, this additional HDI stress keeps the ductility unchanged by offsetting the decreased HDI stress arising from the hetero-deformation between recrystallized (RX) and non-recrystallized (NRX) areas. The unchanged yield strength comes from the increased strengthening effects of the lamellar precipitates and grain boundaries. We also confirmed that the discontinuous coarsening contributes to the formation of heterogeneous precipitates. These findings would open a new pathway for enhancing the consistency and processability of hetero-structured alloys and thus promote their broader industrial applications.

### 1. Introduction

High entropy alloys (HEAs) expand the design space of metallic materials enormously, allowing metallurgists to develop stronger and more ductile alloys with multi-principal-element ideas (George et al., 2020; Li et al., 2023; Shen et al., 2024, 2023; Wei et al.,

\* Corresponding authors.

E-mail addresses: [zhijwang@nwpu.edu.cn](mailto:zhijwang@nwpu.edu.cn) (Z. Wang), [fenghe1991@nwpu.edu.cn](mailto:fenghe1991@nwpu.edu.cn) (F. He).

2022b, 2022a, 2020; Yeh et al., 2004). In addition to innovative multi-principal compositions, a novel microstructure design strategy called heterogeneous microstructure (HGS) has been introduced into HEAs to improve their strengths and ductility recently (Fu et al., 2022; Hasan et al., 2019; Liu et al., 2024; Ma and Wu, 2019; Sathiyamoorthi and Kim, 2022; Wang et al., 2024; Yang et al., 2018; Zhang et al., 2023a). As a typical heterogeneous microstructure, the partial-recrystallization microstructure obtained from cold-rolling and subsequent annealing has achieved excellent strength-ductility combinations in HEAs (Jo et al., 2017; Shukla et al., 2018; Slone et al., 2019; Wu et al., 2022, 2019a; Yang et al., 2018). Moreover, partial recrystallization is one of the cheapest and most efficient processing methods to obtain HGS from large bulk alloys, which is thus highly propagable for industry applications (Du et al., 2020; Fan et al., 2020; He et al., 2021b; Li et al., 2021b; Slone et al., 2019; Wu et al., 2019a; Yu and Luo, 2019). However, in most HEAs, the mechanical properties change dramatically with different recrystallization volume fractions (Luo et al., 2023; Slone et al., 2019), which makes it challenging to acquire the desired HGS and limits the processing windows of partially recrystallized HEAs. Therefore, obtaining the unchanged mechanical properties is of vital importance for partially recrystallized HEAs.

The mechanical properties of the single-phase partially recrystallized HEAs are mainly dominated by the recrystallization volume fraction, following a classical mixture rule (Li et al., 2021; Ming et al., 2019; Slone et al., 2019). In contrast, in the multi-phase partially recrystallized HEAs, the morphology of precipitates can also significantly affect the strength and ductility, offering another way of tuning mechanical properties (An et al., 2023; Dasari et al., 2021; Fan et al., 2022, 2020; Gwalani et al., 2021; He et al., 2021; Ming et al., 2018; Yang and Kim, 2022; Zhang et al., 2024). For example, it is found that the transition from sphere to rod increases the yield strength from 1.0 to 1.6 GPa while the ductility exceeds 10 % (Gwalani et al., 2021). Similarly, alloy with ellipsoid or lamellar precipitates exhibits higher strength and ductility (~2.0 GPa and 16 %) than those of the same HEA with spherical precipitates (~0.5 GPa and 15 %) (Fan et al., 2020). Furthermore, recent works showed that the mechanical properties are almost unchanged when the precipitates distributed heterogeneously in partially recrystallized HEAs. It is reported that the tensile properties slightly changed with recrystallization fractions in 50 % cold-rolled HEAs with heterogenous precipitates (Yang et al., 2022). Similar results of unchanged mechanical properties were also observed in partially recrystallized HEAs with 40 % ~70 % pre-strain by Fang et al. (2022a). Yang and Kim (2022) found that alloys exhibit similar ultimate tensile strengths and total elongations after being annealed for 2 h, 5 h, and 10 h with different recrystallization fractions. However, the underlying mechanisms of the unchanged mechanical properties are still unclear, and the formation mechanism of such unique heterogenous precipitates is under debate.

In this study, we investigated the mechanical properties of alloy,  $\text{Ni}_2\text{CoCrFeTi}_{0.24}\text{Al}_{0.2}$ , with heterogeneous precipitates and different recrystallization fractions (RX%). The results show the tensile properties of the current HEAs are unchanged when the RX% changes from ~21 % to ~72 %. With the aid of micro-digital image correlation ( $\mu$ -DIC), we uncovered the origin of the unchanged ductility. Besides, by integrating high-resolution scanning electron microscopy (HR-SEM), electron backscattered diffraction (EBSD), and transmission electron microscopy (TEM), we confirmed that discontinuous coarsening is responsible for the formation of heterogeneous precipitates.

## 2. Experiments

### 2.1. Materials fabrication and sample preparation

In this work, high-entropy alloy ingot was prepared by vacuum arc-melting in an argon atmosphere with a nominal composition,  $\text{Ni}_2\text{CoCrFeTi}_{0.24}\text{Al}_{0.2}$ . The composition elements were supplied by Zhong Nuo Advanced Material (Beijing) Technology Co., Ltd with 99.95 wt.% purity. We remelted the ingot at least four times to promote the chemical homogeneity and dropped it into a water-cooled copper mold with a dimension of  $50 \times 10 \times 5 \text{ mm}^3$  (Cui et al., 2023; Liu et al., 2022). Alloys were next homogenized at 1200 °C for 2 h followed by cold rolling with a total thickness reduction of ~70 %. According to our previous works (Yang et al., 2021; He et al., 2021b), we selected 800 °C as the annealing temperature to obtain the concurrent recrystallization and precipitation microstructures. Meanwhile, 75 min, 90 min and 105 min were further chosen as the annealing time to obtain different recrystallization fractions. All annealing treatments were conducted in air followed by water quenching. Detailed thermal-mechanical processing routes are shown in Fig. S1.

### 2.2. Mechanical property testing

We focused on the room-temperature tensile mechanical property of the concurrent recrystallization and precipitation high-entropy alloys (CHEAs). The dog-bone-shaped tensile samples were cut from the annealed sheet by electron discharge machine (EDM) with a gauge length of 12.5 mm and width of 3 mm. We ground the surface by 240#, 800#, 1500#, 2500# SiC papers and carried out the quasi-static tensile tests on the TSMT universal tensile machine (TSMT EM6. 504) with a strain rate of  $10^{-3} \text{ s}^{-1}$ . We tested three samples to verify the reproducibility of the uniaxial tensile data. To further characterize the hetero-deformation induced stress, the same size samples were used for the load-unload-reload (LUR) tensile test. During the loading/reloading stages, we set the strain rate,  $1 \times 10^{-3} \text{ s}^{-1}$  by the strain-control mode. During the unloading stage, we used the stress-control mode with  $10 \text{ MPa}\cdot\text{s}^{-1}$ . Three samples were also tested to verify the reproducibility of the LUR test data.

### 2.3. Microstructural characterization

Scanning electron microscope (SEM, TESCAN AMBER) was firstly used to characterize the morphologies of precipitate in different areas using the in-beam SE detector. EBSD (Oxford Instrument, Symmetry S2) was performed to calculate the recrystallization fractions

with a data post-processing software (Aztec Crystal). We quantified three EBSD images (view field 500  $\mu\text{m}$ ) to obtain a reliable recrystallization volume fraction for each specimen. X-ray diffraction (XRD) analysis utilized Cu radiation was conducted from 20 to 100° on the Rigaku Dmax-2550 and Jade 6.0 software was used to analyze the XRD patterns. Lattice structure and composition analysis of nano-precipitate were conducted via transmission electron microscope (TEM, Talos F200X) operating at 200 keV, including bright-field (BF) imaging, dark-field (DF) imaging and selected area electron diffraction (SAED). Thin-foil for TEM observation was firstly ground to a thickness of 50  $\mu\text{m}$ , punched into disks with 3 mm diameter, and finally thinned through twin-jet polishing using a solution of 10 vol.% perchloric acid and alcohol at -30 °C with 50 V.

#### 2.4. Strain partition measurement by micro-digital image correlation ( $\mu$ -DIC)

The *in-situ*  $\mu$ DIC was carried out in the chamber of SEM and used to capture the strain partition behavior of the CHEAs. The *in-situ* tensile specimen was also cut by EDM with a gauge length of 4 mm and width of 2 mm. Surface of the specimen was polished and dispersed with a homogeneously SiO<sub>2</sub> monolayer. Inspired by the work (Wei et al., 2022), we performed the *in-situ* tensile test on the Kammerath & Weiss micro-test system equipped with a 5 kN load cell with a strain rate of 10<sup>-3</sup> s<sup>-1</sup>. Initial microstructures of the target area are shown in Fig. S2. During the tension process, in-beam SE images with 8192 × 8192 pixels resolution (view field 50 × 50  $\mu\text{m}$ ) were recorded at every 0.5 % strain incrementation (The actual strain was further corrected by wider view field images of the gauge, 6000  $\mu\text{m}$ ). For the data analysis, we used the software, GOM correlate, to create the surface component (<https://www.gom.com/en/products/gom-correlate>), and set the square facet size with 54 × 54 pixels applied for DIC analysis, resulting in a spatial resolution ~330 × 330 nm which is high enough to reveal the strain partition in this work.

### 3. Results

#### 3.1. Partially recrystallized microstructures

We first carried out an EBSD analysis to characterize the recrystallization volume fractions of samples annealed at different time. As demonstrated in Fig. 1(a-c), three samples are partially recrystallized and the RX% values are measured, ~21 %, ~57 %, and ~72 % respectively by averaging the values of three randomly selected regions of 500  $\mu\text{m}$  × 500  $\mu\text{m}$ . Samples are referred as RX\_21 %, RX\_57 % and RX\_72 % corresponding to the recrystallization volume fractions. Grain sizes are calculated, 0.6  $\mu\text{m}$ , 1.1  $\mu\text{m}$ , and 3.0  $\mu\text{m}$  respectively in the recrystallized region using the subset selection module of Aztec Crystal software. The KAM images are also presented to confirm the partial recrystallization microstructures with the threshold 0 °~3 ° in Fig. 1(d-f). The non-recrystallized (NRX) regions are represented by the highly misoriented regions and decrease with the annealing time, indicating three samples are partially

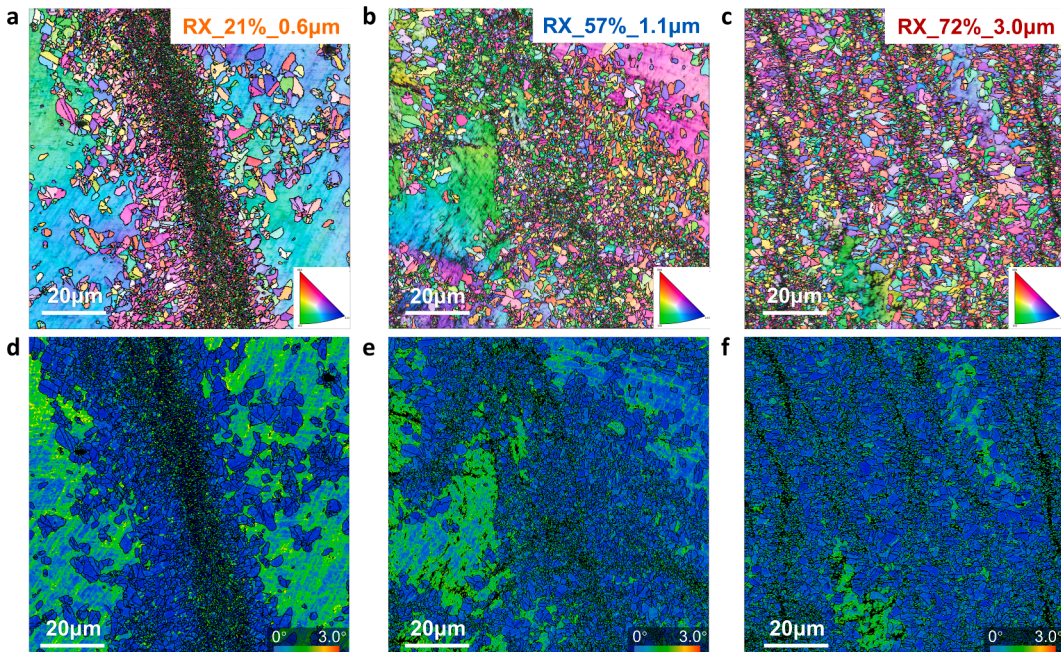


**Fig. 1.** EBSD maps of the heterogeneous microstructure of Ni<sub>2</sub>CoCrFeTi<sub>0.24</sub>Al<sub>0.2</sub> with different recrystallization volume fractions and grain sizes. (a-c) Inverse pole figures (IPF) of alloys with 21 %, 57 %, and 72 % recrystallization fractions and grain sizes in RX area are 0.6  $\mu\text{m}$ , 1.1  $\mu\text{m}$ , and 3.0  $\mu\text{m}$  respectively, (d-f) Kernel average misorientation (KAM) maps of the alloys with different recrystallization fractions, showing that the proportion decreases for the NRX areas with high KAM value.

recrystallized with different RX % again.

### 3.2. Heterogeneous precipitates

Next, high-resolution SEM imaging was performed to clarify the characteristics of precipitates in RX and NRX zones of the concurrent recrystallization and precipitation high-entropy alloys (CHEAs) in Fig. 2. As for RX\_21 % in Fig. 2(a), the RX region shows sub-micrometer precipitates with bright contrast. Differently, the precipitates in the NRX zone are not observable under the same imaging condition. High-resolution SEM images show that there are also precipitates in NRX regions. Note that morphologies of precipitate in the RX region and NRX region are completely different, i.e., precipitates exhibit lamellar shape with heterogeneous size distribution in the RX zone while precipitates exhibit spherical shape with homogeneous size distribution in the NRX zone (Fig. 2(b)(c)). When the RX % increases, the lamellar precipitates also increase and gradually occupy the whole sample in Fig. 2(a)(d)(g). From the enlarged Fig. 2 (b)(e)(h), the lamellar precipitates exist in each RX grain and some smaller precipitates exist at the center of the RX grain with a nearly spherical shape. In the NRX areas, the features of precipitates almost do not change with the increase of RX% in Fig. 2(c)(f)(i),

Fig. 3 shows the XRD and TEM results. Considering the larger detection area size and faster analysis efficiency of XRD, we used XRD to identify the phase variety of precipitates firstly. From Fig. 3(a), we found three samples exhibit the same lattice structure of face-centered cubic (FCC) with some asymmetry in main diffraction peaks. In Fig. 3(b), peak fitting analysis shows that there should be the L1<sub>2</sub> phase in FCC matrix and the misfit between the two phases is close to ~0.15 % which is usual in L1<sub>2</sub>-strengthened alloys. The L1<sub>2</sub> phase was further identified by TEM in Fig. 3(c). In regard to the NRX region, the high density of sphere L1<sub>2</sub> precipitates is proved by the BF image and the superlattice diffraction spots in SADP (Fig. 3(e)). Besides, high density of defects, e.g., deformation twins, are also detected by DF image and corresponding diffraction spots in SADP (Fig. 3(d)). In the RX region, obvious lamellar precipitates are

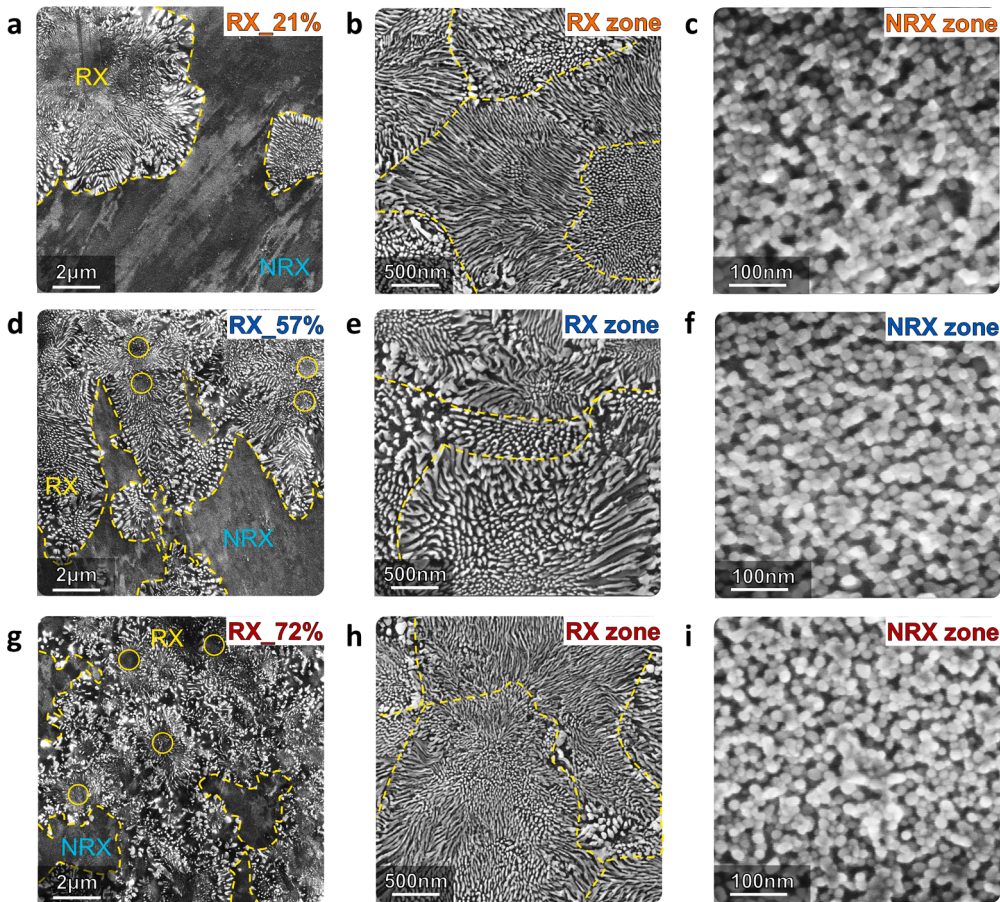


**Fig. 2.** Morphologies of representative RX and NRX zones and precipitates in RX and NRX zones. (a-c) low recrystallization fraction (LRX) microstructures, (a) bright areas represent recrystallized areas (~21 %), and dark areas represent non-recrystallized areas, the contrast changes caused by deformation defects. (b) and (c) display the characteristics of precipitate in recrystallized (RX) areas and non-recrystallized (NRX) areas, respectively, lamellar precipitates in RX areas and sphere precipitates in NRX areas. (d-f) medium recrystallization fraction (MRX) microstructures, (d) a percentage of RX areas are increasing to 57 %. Similarly, (e) and (f) exhibit the lamellar and sphere precipitates in RX and NRX areas, respectively. (g-i) high recrystallization fraction (HRX) microstructures, (g) shows the increased recrystallization fraction up to 72 %, (h) and (i) represent the lamellar precipitates and the sphere precipitates, respectively.

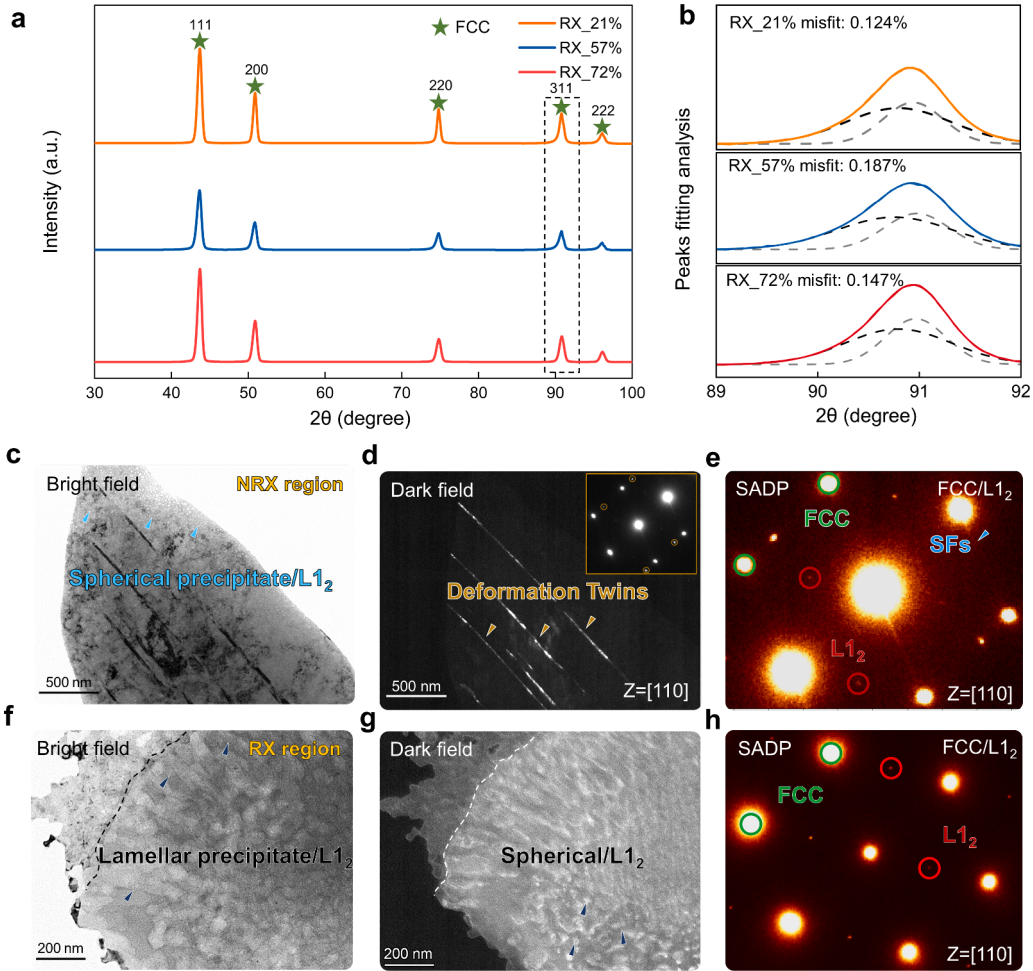


**Fig. 3.** Phase identification, misfit calculation, and precipitates structure of CHEAs. (a) XRD pattern of RX\_21 %, RX\_57 %, and RX\_72 % samples, all samples show a typical FCC structure without different lattice-type phases occurring. (b) peaks fitting analysis of (311) peaks in (a) by a fine scanning at 0.09 °/min. (c) bright field (BF) image of the spherical precipitate characteristics in the NRX region. (d) dark field (DF) image proves the existence of preserved deformation twins in NRX region. (e) selected area diffraction pattern (SADP) of the NRX region. (f) BF image of the lamellar precipitate characteristics in RX region, (g) DF image shows the spherical precipitate characteristics in RX region. (h) SADP of the RX region.

displayed in both BF and DF images. At the end of lamellar precipitates, spherical precipitates can also be observed in Fig. 3(f)(g), consistent with Fig. 2(b)(e)(h). The corresponding SADPs show that both lamellar and particle-like precipitates are the L1<sub>2</sub> structure in Fig. 3(h). The composition maps in Fig. S3 show that these L1<sub>2</sub> precipitates are rich in Ni, Ti, and Al elements.

### 3.3. Mechanical properties

Fig. 4 presents the room-temperature tensile properties of the samples with different recrystallization volume fractions. It is surprisingly found that the stress-strain curves of the three HEAs are almost unchanged, i.e., yield strength (YS) is ~1.3 GPa, ultimate tensile strength (UTS) is ~1.5 GPa and total elongation is approximate 20 % including the uniform elongation and post-necking elongation of three alloys in Fig. 4(a). Tensile test of each alloy has been carried out three times to keep the credibility of the experimental results, as shown in Fig. S4. From Fig. 4(b), although samples exhibit different post-necking elongation with different recrystallization fractions, i.e., 5.6 %, 3.4 %, and 4.7 %, the uniform elongation values are very close (~15 %). The similar uniform elongations are well explained by the similar strain hardening behaviors of the three alloys, (Fig. 4(c)). These observations differ from the single-phase HEAs completely, whose mechanical properties change largely with recrystallization fractions (Slone et al., 2019).

### 3.4. Deformation mechanisms

After tensile testing, the fracture morphologies and the GND distribution are shown in Fig. 5. The IPF and KAM images clearly delineate the RX and NRX areas based on grain orientation in Fig. 5(a-c). All the KAM images show that the RX regions exhibit higher

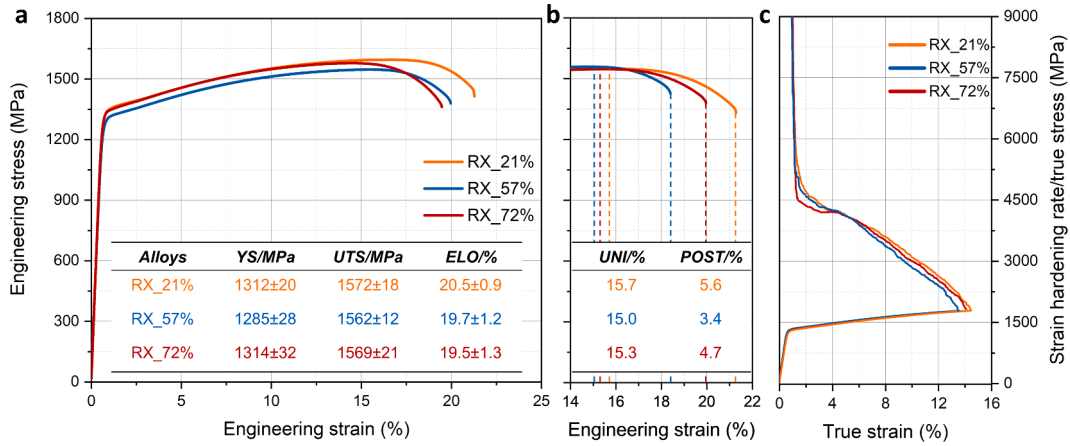


**Fig. 4.** Tensile mechanical properties and strain hardening ability of CHEAs with different recrystallization fractions. (a) RX\_21 %, RX\_57 %, and RX\_72 % show almost unchanged tensile properties, yield strength (YS) ~1300 MPa, ultimate tensile strength (UTS) ~1560 MPa, total elongation (ELO) ~20 %. (b) post-necking behaviors of three alloys includes uniform elongation (UNI) and post necking elongation (POST), (c) the strain hardening rate curves show almost same tendency.

misorientation than the NRX regions. Specifically, the RX\_21 % shows obvious strain accumulation in the RX regions and planar deformation bands in the NRX regions in Fig. 5(a). In contrast, the deformation bands are curved and shorter in RX\_57 % in Fig. 5(b). For the RX\_72 %, the deformation bands are even more curved and denser with reduced lengths, indicating that the NRX areas are divided more dispersedly by the RX areas in Fig. 5(c). It is believed that these deformation bands are related to the re-activation of defects in the NRX areas (Kaushik et al., 2021; Wu et al., 2019b). To further elucidate the deformation mechanisms, we quantified the GND density from the KAM images and obtained GND density from the subsets of RX and NRX regions (Liu et al., 2020). In Fig. 5(d), the overall GND densities of RX\_21 % and RX\_72 % are similar after fracture while RX\_57 % shows the highest value after fracture. Moreover, a smaller recrystallized volume fraction is correlated with a higher GND density in RX areas (Fig. 5(e)). Conversely, in NRX areas, the GND density is the lowest for the RX\_21 % while the GND densities of the 57 % and 72 % samples are close (Fig. 5(f)). All samples show hetero-deformation characteristics, i.e., the RX and NRX areas deformed heterogeneously based on the KAM images and the average GND density.

We measured the hetero-deformation induced (HDI) stress of the three HEAs by loading-unloading-reloading hysteresis loops to understand the heterogeneous deformation mechanisms, as shown in Fig. 6. Counter-intuitively, three HEAs exhibit almost identical hysteresis loops with different recrystallization volume fractions (Fig. 6(b)). Using the methodology proposed by Yang et al. (2016), we showed the evolution of HDI stress with true strain in Fig. 6(c). The similar HDI stress evolution (from ~750 MPa to ~1100 MPa)

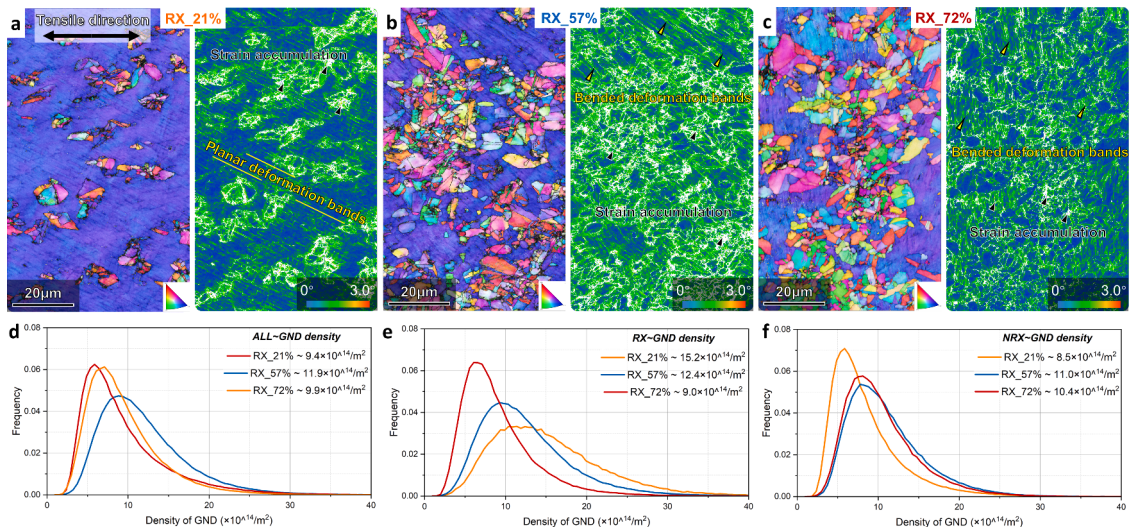


**Fig. 5.** Fracture morphologies of RX and NRX regions with GND density distribution of different recrystallized volume fractions CHEAs. (a) IPF and KAM map of the RX\_21 %, (b) IPF map and KAM map of the RX\_57 %. (c) IPF map and KAM map of the RX\_72 %. (d) Comparison of overall GND density of three samples after fracture. (e) Comparison of GND density in the RX areas, (f) Comparison of GND density in the NRX areas.

indicates identical hetero-deformation hardening contributions to ductility in HEAs with different RX%. Such a novel phenomenon has never been found in either partially recrystallized single-phase alloys or alloys with artificially designed heterostructures (Liu et al., 2020; Sloane et al., 2019). By coupling the EBSD and LUR results, we here concluded that the similar tensile properties of HEAs are due to the unique hetero-deformation mechanisms. A detailed discussion is provided about the physical mechanisms in the following part.

#### 4. Discussion

##### 4.1. Origins of the same ductility for HEAs with different recrystallization fractions

To clarify the origin of the similar HDI stress that causes the unchanged ductility in these HEAs, we need to answer the following two questions:

- 1) What are the sources of HDI stress?
- 2) How does the source of HDI stress evolve with varying RX%?

To answer these, we performed variate-controlled LUR tests and  $\mu$ -DIC experiments to uncover the hetero-deformation behaviors and then modified a GND-based model to understand the HDI stress evolution with RX%.

###### 4.1.1. Hetero-deformation behaviors

Generally speaking, the partially recrystallized microstructures exhibit strong mechanical incompatibility between RX and NRX areas. The hetero-deformation around the interface of two areas has been proven to be an HDI stress source (Cao et al., 2021; Fang et al., 2019; Wu et al., 2015). Different from single-phase HEAs, here we introduce precipitates into both RX and NRX areas, affecting the overall hetero-deformation behavior (Xu et al., 2022). Next, the variate-controlled experiments were conducted to reveal the effect of these precipitates on HDI stress based on our previous work (Yang et al., 2021). Firstly, as the partially recrystallized matrix alloy, the single-phase Ni<sub>2</sub>CoCrFe is designed to investigate the effect of precipitates on overall HDI stress with a similar RX% (~61%). Secondly, a fully recrystallization HEA with homogeneous-distributed precipitates is also designed to compare the HDI stress of precipitated alloys with heterogeneous distribution and homogeneous distribution. Results of the designed LUR tests are shown in Fig. 7. Obviously, CHEAs exhibit the largest size of loops among all tested alloys in Fig. 7(b). Specifically, the HDI stress value increases from 750 MPa to 1100 MPa for the CHEAs while the value remains at 500 MPa for the single-phase matrix alloy and increases slightly from 450 MPa to 750 MPa for the fully recrystallization HEAs (Fig. 7(c)). The dramatically increased value indicates that not only does the introduction of precipitation increase the HDI stress, but also the heterogeneous distribution of precipitates increases the overall HDI stress further. Therefore, there must exist a new hetero-deformation source related to the heterogeneously distributed precipitates in addition to the hetero-deformation between RX and NRX areas from the variate-controlled experiment results of HDI stress.

To prove above viewpoint, we used  $\mu$ -DIC to analyze the hetero-deformation behaviors quantitatively. Fig. 8 captures the grain scale hetero-deformation with a 50  $\mu\text{m} \times 50 \mu\text{m}$  view field in RX\_21 %. At the global strain of 0.17 %, the overall strain distribution is relatively uniform in Fig. 8(a). The strain partitioning is not obvious between the RX region and NRX region, showing that both regions are in the elastic deformation stage. At a strain of 0.69 %, strain begins to accumulate locally, which is a typical characteristic feature of hetero-deformation (Nie et al., 2023; Park et al., 2018; Sloane et al., 2019). At the same time, strain accumulation bands appear in the NRX region which is caused by the reactivation of pre-existing defects (Wu et al., 2019a). When the strain increases to 0.86 %, more strain accumulated points (black triangle marked) appear and strain accumulation bands are more obvious. At the global strain of 1.20 %, more pronounced strain partitioning behavior appears between RX regions and NRX regions. Fig. 8(b) exhibits the initial microstructure for line strain analysis including the RX area (red) and the NRX area (blue), which exhibits a uniform distribution of dispersed particles on the surface. To compare the strain partitioning behavior more quantitatively, linear strain analysis has been carried out in Fig. 8(c). Apparently, the average strain in the RX region is always larger than that in near NRX region as the dot lines shown. Therefore, a significant strain gradient is generated around the boundary, leading to HDI hardening by the GND accumulation (Yang

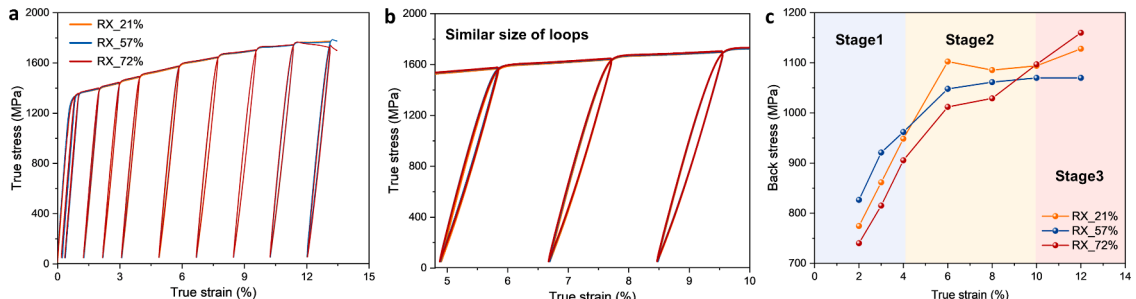


**Fig. 6.** Load-Unload-Reload (LUR) curves and HDI stress analysis of CHEAs with different recrystallization fractions. (a) LUR curves of RX\_21%, RX\_57 %, and RX\_72 % CHEAs, (b) magnified loops of local LUR curves of three alloys, (c) HDI stress evolution at different deformation stages of CHEAs.

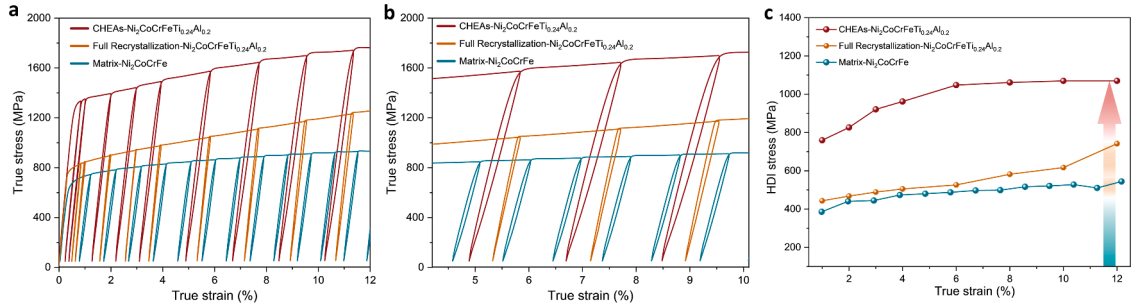


**Fig. 7.** Comparison of HDI stress between HGS matrix, Ni<sub>2</sub>CoCrFe, the homogeneous-precipitated, and the heterogeneous-precipitated HEAs, Ni<sub>2</sub>CoCrFeTi<sub>0.24</sub>Al<sub>0.12</sub>, (a) LUR curves of CHEAs and the corresponding FCC matrix, Ni<sub>2</sub>CoCrFe, with the same recrystallization fraction and the homogeneous-precipitated HEA with full recrystallization microstructure, (b) magnified loops of LUR curves of three samples, (c) evolution of HDI stress in above three samples.

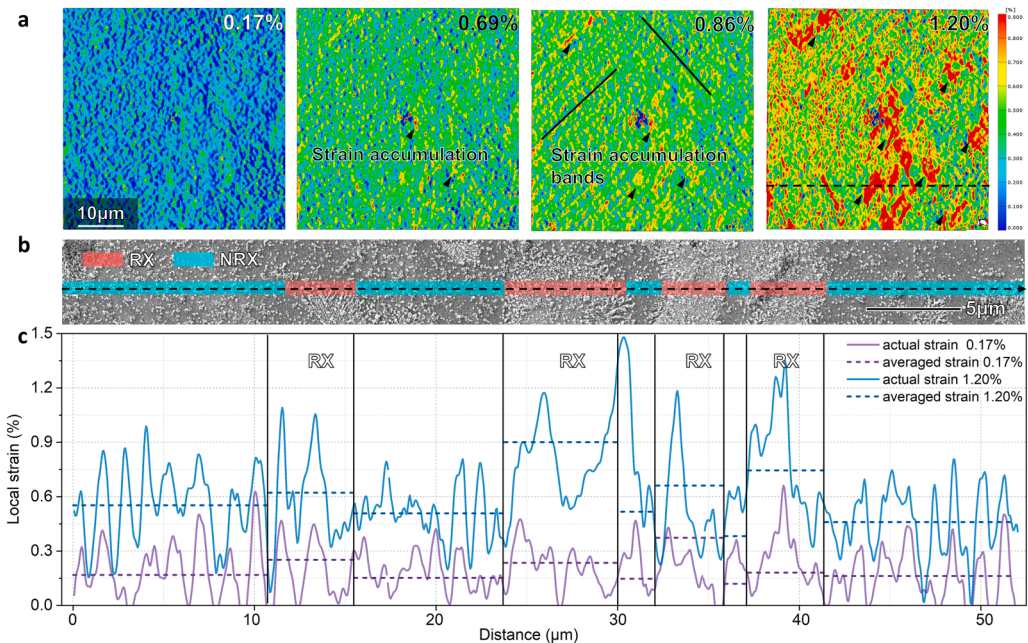


**Fig. 8.**  $\mu$ -DIC analysis of the strain partition behavior between the recrystallized and non-recrystallized regions of the partially recrystallized structure at different global strains, (a) Strain distribution maps under global strains of 0.17 %, 0.69 %, 0.86 %, and 1.20 % after strain correcting, (b) real microstructures corresponding to the line strain distribution analysis, where the red area represents recrystallized areas and the blue area represents non-recrystallized areas, (c) linear strain distribution in the recrystallized and non-recrystallized areas under global strains of 0.17 % and 1.20 %. The dot lines represent the average strain and the solid lines represent the actual strain. (For interpretation of the references to colour in this figure legend, the reader is referred to the web version of this article.)

et al., 2018). Intriguingly, there seems to exist a more obvious strain gradient from the sharper variation of local strain inside the RX region. The high-resolution EBSD maps also show a heterogeneous distribution of misorientation in the RX area, as shown in Fig. S5. Inspired by the heterogeneous precipitates in the RX area in Fig. 2(b), we speculate that this strain gradient may be related to the hetero-deformation between the areas with lamellar precipitates and spherical precipitates. Next, more local high-resolution  $\mu$ -DIC is used to prove this hypothesis.

The strain maps show that the RX region produces obvious strain accumulation bands at 0.17 % macroscopic deformation in Fig. 9 (a). This indicates that the plastic deformation already occurs before the 0.2 % global strain, which proves the HDI strengthening effect (Chou et al., 2022). As the global strain increases from 0.69 % to 0.86 %, local strain tends to accumulate in the RX grain. The morphology of the RX grain can be found in Fig. S2 and grain boundary is circled by the black line in the 1.20 % strain map in which the local strain is more severe around the RX grain boundary areas. Next, aiming to quantitatively uncover the intragranular strain partitioning behavior, the linear strain analysis was carried out as the dot line shown in the 1.20 % strain map. The corresponding microstructure for linear strain analysis is shown in Fig. 9(b). It is worth noting that there are two shapes of precipitates in RX areas. One is spherical shape in the center of the RX area with a smaller size of  $\sim 10$  nm. The other is lamellar shape around the grain

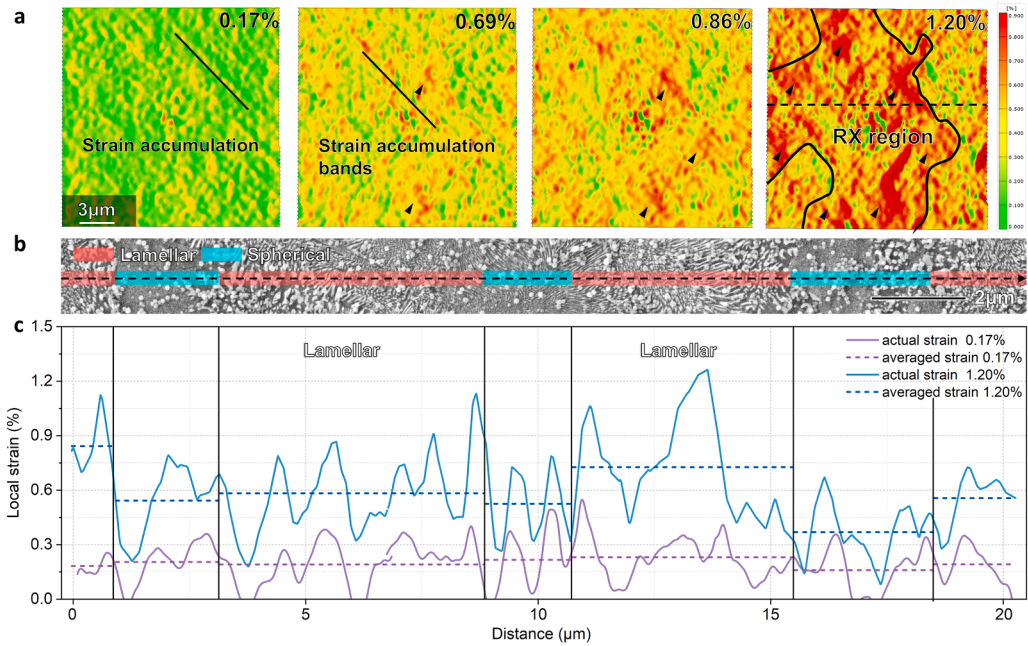


**Fig. 9.**  $\mu$ -DIC analysis of the strain partition behavior of the regions between lamellar precipitate areas and spherical precipitate areas inside the recrystallized region at different global strains. (a) strain distribution map inside a recrystallized grain under the global strains of 0.17 %, 0.69 %, 0.86 %, and 1.20 %. The black curve circled area represents the recrystallized grain. (b) microstructure corresponding to the linear strain analysis, the red area represents the lamellar precipitate area while the blue area represents the spherical precipitate area. The precipitates show a lamellar-sphere-lamellar shape transition from 3  $\mu$ m to 15  $\mu$ m, (c) linear strain distribution corresponding to the lamellar precipitate area and spherical precipitate area under the global strains of 0.17 % and 1.20 %. The dot lines represent the average strain and the solid line represent the actual strain. (For interpretation of the references to colour in this figure legend, the reader is referred to the web version of this article.)

boundary with a larger size  $\sim 80$  nm. Due to these heterogenous precipitates, detectable strain partition exists inside the RX regions between lamellar precipitate area and spherical precipitate area (Fig. 9(c)). Apparently, the average strain in the lamellar region is always larger than that in near spherical region as the dot lines shown.

As far as we know, the new strain partition pattern is first observed and verified. Thus, we think this hetero-deformation is a new HDI stress source in CHEAs which definitely contributes to an extra HDI hardening effect in Fig. 7. From the above  $\mu$ -DIC results, we successfully verified there are two HDI stress sources, i.e., hetero-deformation between RX and NRX areas and hetero-deformation between lamellar and spherical precipitates regions. The morphology heterogeneity related with the generation of two HDI stresses varies during annealing. It is reasonable to hypothesize that two HDI stresses transform to each other with the increase of RX% which results in the unchanged overall HDI stress.

#### 4.1.2. HDI stress evolution with RX%

In the partially recrystallized microstructures, the HDI stress evolution should be considered individually in RX and NRX areas since the variation tendencies are different (Li et al., 2022). In the NRX area, the high-density GND shows a decreased tendency for the re-activation of pre-existing defects during the deformation. In contrast, GND density shows an increased tendency in the RX area (Wu et al., 2019a). It is the variation of GND density that determines the actual HDI stress. Therefore, we calculated two HDI stresses in RX and NRX areas respectively using the model in Eq. (1) (Li et al., 2021; Li and Soh, 2012; Wang et al., 2022b, 2022a). Due to the uniaxial tensile condition, here we only consider the tensile direction,  $x$ . Besides, the accumulation length of GND,  $R$ , is assumed to equal the value of  $\partial x$ , both of which represent the size of the unit GND accumulation domain. Based on above assumptions, an expression of the simplified HDI stress equation is shown in Eq. (2) (Wang et al., 2022b).

$$\sigma_{HDI} = \frac{\sqrt{3}}{8} \frac{\mu b k R^2}{(1-\nu)} \sqrt{\left(\frac{\partial \rho}{\partial x}\right)^2 + \left(\frac{\partial \rho}{\partial y}\right)^2 + \left(\frac{\partial \rho}{\partial z}\right)^2}, \quad (1)$$

$$\sigma_{HDI} = \frac{\sqrt{3}}{8} \frac{\mu b k R^2}{(1-\nu)} \sqrt{\left(\frac{\partial \rho}{\partial x}\right)^2} = \frac{\sqrt{3}}{8} \frac{\mu b k R^2}{(1-\nu)} \frac{\partial \rho}{\partial x} = \frac{\sqrt{3}}{8} \frac{\mu b k R}{(1-\nu)} \Delta \rho, \quad (2)$$

where  $\sigma_{HDI}$  is HDI stress,  $\mu$  is the shear modulus  $\sim 84$  GPa,  $b$  is the burgers vector  $\sim 0.253$  nm,  $\nu$  is Poisson ratio  $\sim 0.31$ , and  $k$  is the GNDs configuration correction factor  $\sim 0.42$ . The variation of GND density can be obtained from the KAM images,  $\Delta \rho$ , summarized in Table.

S1.  $R$  is the radius of GND domain corresponding to the effective GND accumulation length,  $l_{\text{eff}}$  (Wang et al., 2022b; Zhang et al., 2023b). Given that the deformation mechanisms are different for grains with different sizes, the effective GND accumulation lengths,  $l_{\text{eff}}$ , are also considered separately in RX and NRX areas (Britton and Wilkinson, 2012; Guo et al., 2020; Schneider et al., 2020; Wagner and Laplanche, 2023). For the grain with small size, there exists an overlap for the GND domains and no obvious GND accumulation can be found in the interior of larger-size grain (Guo et al., 2022; Huang et al., 2018; Wang et al., 2023; Wu et al., 2023). Here, we hypothesized that there must exist a critical length value,  $l$ . When the grain size is smaller than this value, the GND domains overlap, and overlap disappears when the grain size is larger than the value. Therefore, the effective GND accumulation length,  $l_{\text{eff}}$ , is modified to describe the actual size of dislocation affected zone, as shown in Eq. (3) (Wang et al., 2023).

$$\sigma_{\text{HDI}} = \frac{\sqrt{3}}{8} \frac{\mu b k l_{\text{eff}}}{(1 - v)} \Delta \rho, \quad l_{\text{eff}} = \begin{cases} d_{\text{area}}, & l > d_{\text{RX}}, \\ l, & l < d_{\text{RX}} \end{cases}, \quad (3)$$

where  $l = b \cdot (\mu / \sigma_{0.2})^2$  following Ref. (Huang et al., 2018).  $l$  is calculated to be  $\sim 3.0 \mu\text{m}$ .  $\mu$  is the shear modulus.  $b$  is the burgers vector.  $\sigma_{0.2}$  is the yield strength adopted from our previous work (He et al., 2021a). Since the tensile experiment is uniaxial, the overall stress can be obtained by volume averaging over all the components (Li et al., 2017; Wang et al., 2020; Zhao et al., 2021). The global HDI stress,  $\sigma_{\text{HDI,global}}$ , can be approximated as the fraction-weighted average value of HDI stress of the RX area,  $\sigma_{\text{HDI,RX}}$ , and the NRX area,  $\sigma_{\text{HDI,NRX}}$ , as shown in Eq. (4) from (Wang et al., 2019; Zhang et al., 2021).

$$\sigma_{\text{HDI,global}} = RX\% \sigma_{\text{HDI,RX}} + (1 - RX\%) \sigma_{\text{HDI,NRX}}, \quad (4)$$

The calculated HDI stresses were shown in Table 1. With the increase of RX%, HDI stress in the RX area increases continuously from 283 MPa in RX\_21 % to 984 MPa in RX\_72 %. The main reasons for the increase in HDI stress are the increased recrystallization volume fraction and increased GND effective accumulation length. Since the hetero-deformation occurs between lamellar and spherical precipitate regions in the RX area, the related HDI stress contribution increases with the increase of RX%. Besides, it is found that the GND density variation in NRX area decreases from  $2.5 \times 10^{14}/\text{m}^2$  to  $1.2 \times 10^{14}/\text{m}^2$  initially and then increases to  $1.5 \times 10^{14}/\text{m}^2$ . The calculated HDI stress of the NRX area decreases from 856 MPa to 182 MPa which is caused by the decreased non-recrystallization volume fraction. Given this HDI stress of the NRX areas comes from the hetero-deformation between the RX and NRX areas, it is reasonable to deduce that this HDI stress source always decreases with the increase of RX%. The overall HDI stress is composed of the above two HDI stress sources in Table 1. The calculated values show good consistency with the experimental values in Fig. 10. Besides, the consistent HDI stresses also verified the applicability of the model by comparing the experiment and calculation values of single-phase HEAs. Thus, we deduce that two sources of HDI stress compensate each other and keep the HDI stress unchanged with the increase of RX%, contributing to the unchanged ductility in different RX% alloys.

As for the unchanged yield strength, we used EBSD and nanoindentation techniques to correct the strength affected by recovery-induced dislocation annihilation in Fig. S6. Analysis for the detailed strengthening mechanisms is included in Supplementary Materials. As the recrystallized volume fraction increases, the contribution of continuous precipitation and dislocation strengthening gradually decreases in Table. S2. The contribution of lamellar precipitation strengthening and grain boundary strengthening increases constantly. The effects of the above two processes cancel each other out. Therefore, although the recrystallized volume fractions of three alloys are different, the values of yield strength remain unchanged which are close to 1.3 GPa (Fig. S7).

#### 4.2. Formation mechanism of heterogeneous precipitates

In light of the important role of heterogeneous precipitates in the mechanical properties, we here move to reveal the formation mechanism of precipitates. In Fang's and Gwalani's works (Fang et al., 2022b, 2022a; Gwalani et al., 2021), the discontinuous precipitation is responsible for the formation of heterogeneous precipitates. According to Dasari's work, discontinuous precipitation will be retarded if the matrix relieves the supersaturation by precipitation (Dasari et al., 2021). Differently, we found that the heterogeneous precipitates can still be formed in RX area after the NRX area relieved the supersaturation by producing spherical precipitates in Fig. 2(c). Thus, discontinuous precipitation is not able to explain this phenomenon reasonably. In the current study, the overall fraction of precipitate has reached a stable value close to 30 % in Fig. 11(a). This is different from the discontinuous precipitation which the fraction increases from zero to a steady value (Dasari et al., 2021; Manna et al., 2001). Besides, there also exists a huge difference between the sizes of precipitates in two regions (Fig. 11(b)), i.e., the lamellar size of the precipitate ( $\sim 100 \text{ nm}$ ) is about ten times larger than the spherical precipitates ( $\sim 10 \text{ nm}$ ). The discontinuous precipitation process cannot explain the non-continuous variation of the precipitate size (Gwalani et al., 2021). A TEM study is carried out on the RX and NRX boundary to understand the formation mechanisms of the lamellar precipitates. In Fig. 11(c), the L1<sub>2</sub> precipitates exhibit a spherical shape in the NRX region. A

**Table 1**

Comparison of the HDI stress by calculation and experiment methods of partial recrystallization Ni<sub>2</sub>CoCrFe and Ni<sub>2</sub>CoCrFeTi<sub>0.24</sub>Al<sub>0.12</sub>.

Alloys	Calculated result (MPa)	HDI stress of RX (MPa)	HDI stress of NRX (MPa)	Experiment result (MPa)	Error (MPa)
RX_21 %	1139	283	856	1128	10
RX_57 %	1090	868	222	1070	20
RX_72 %	1116	934	182	1160	-44
S_RX_61 %	534	361	173	544	10

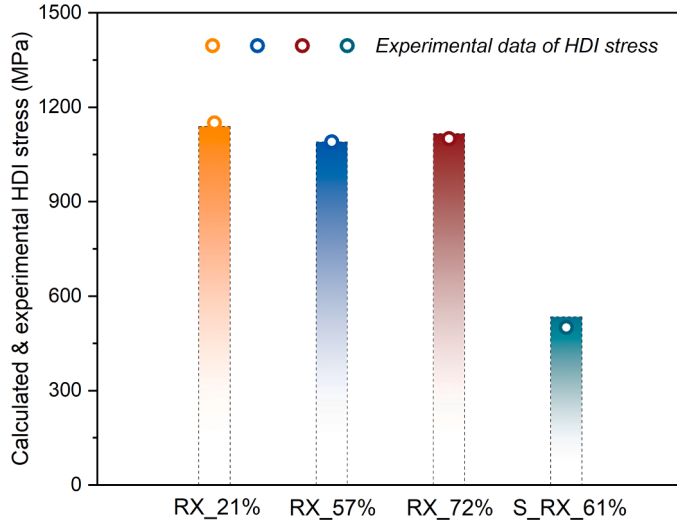


**Fig. 10.** Comparison of the HDI stress by calculation and experiment methods of partial recrystallization  $\text{Ni}_2\text{CoCrFe}$  and  $\text{Ni}_2\text{CoCrFeTi}_{0.24}\text{Al}_{0.12}$  with different recrystallization fractions. The circles represent the experiment data of HDI stress while the columns in histogram represent the calculated HDI stress. S\_RX\_61 % represent the single-phase high-entropy alloy,  $\text{Ni}_2\text{CoCrFe}$ , with 61 % recrystallization volume fraction.

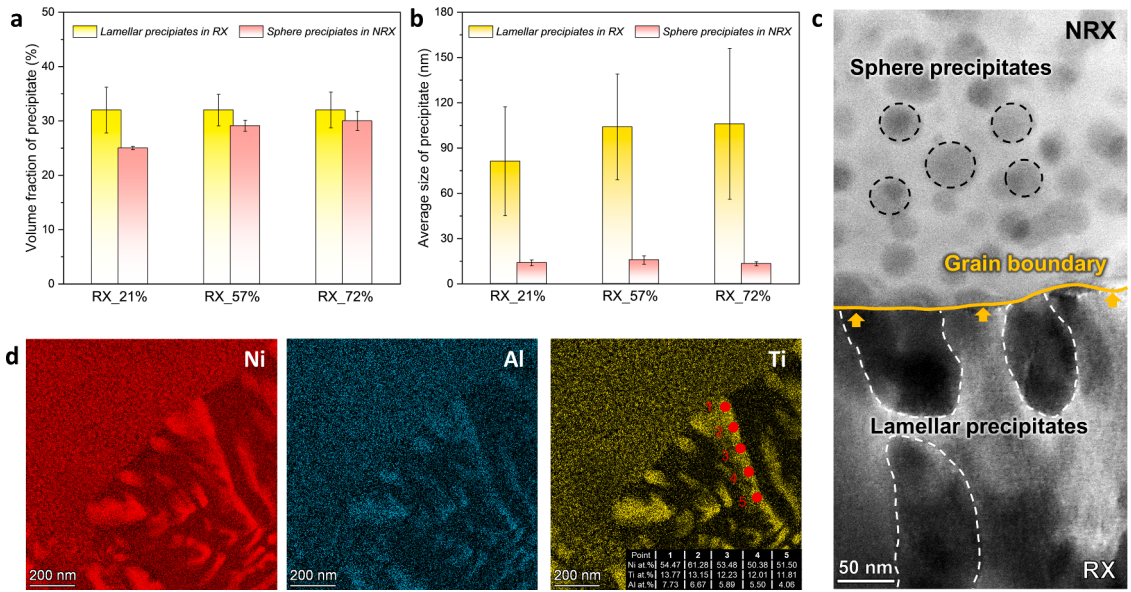


**Fig. 11.** Statistical characteristics, morphologies, and composition maps of precipitates located at the two sides of the moving grain boundary. (a) and (b) illustrate the volume fraction and size of lamellar and spherical precipitates of RX\_21 %, RX\_57 %, and RX\_72 % samples, (c) HADDF maps of the precipitates morphologies around two sides of the boundary of RX area and NRX area, (d) displays STEM-EDS maps of lamellar precipitates in RX area, which is enriched in Ni, Al, and Ti elements.

transformation of spherical shape to a lamellar shape occurs after the sweeping of NRX by the moving RX boundary. Noteworthily, the concentration of the solute elements, Ti, and Al, shows a decreasing tendency from the boundary to the interior (insert of Ti map), as shown in Fig. 11(d). This discontinuity of concentration indicates that the formation of lamellar precipitates is controlled by a discontinuous solute-diffusion process. We have known that these precipitates are  $\text{L1}_2$  phase by XRD and TEM analysis in Fig. 3 and the volume fractions of precipitates are similar and unchanged during annealing, which is a typical feature of a coarsening process for precipitate (Chellman and Ardell, 1974; Manna et al., 2001). Therefore, we conclude that the heterogeneous precipitates come from the discontinuous coarsening of the  $\text{L1}_2$  phase in the current study.

We sketched the discontinuous coarsening process in Fig. 12. Once the grain boundary meets the spherical  $\text{L1}_2$  phase in NRX area in Fig. 11(c), particles on the boundary show faster coarsening rates and larger sizes than those in the interior of NRX area. The decreased trend of solute composition in the inset chart Fig. 11(d), also proves that it is the boundary-assisted diffusion that facilitates the

coarsening behavior. Since the boundary diffusion rate is much higher than the bulk diffusion rate at 800 °C (Fang et al., 2022b), a large size difference exists between two precipitates. Noteworthily, the formation of heterogeneous precipitates comes from the co-evolution of boundary migration rate and diffusion-assisted coarsening rate. The boundary migration rate,  $v_{boundary}$ , is mainly controlled by the follow equation, Eqs. (5) and (6) is given by (Humphreys et al., 2017).

$$v_{boundary} = MP_d \quad (5)$$

$$P_d = apGb^2 \quad (6)$$

where  $M$  is the boundary mobility,  $P_d$  is the net pressure on the boundary,  $a$  is a constant,  $G$  is a shear modulus and  $b$  is the burgers vector. Obviously, the driving force is provided by the dislocation density,  $\rho$ . With the increase of annealing time, the decreased dislocation density will slow the boundary migration rate. Therefore, the boundary migration rate will decrease with the time prolonging. Differently, the boundary-assisted diffusion coarsening rate,  $v_{coarsening}$ , do not change during the annealing process which is mainly controlled by the boundary-assisted diffusion rate and determined by temperature. In the initial stage,  $v_{boundary} > v_{coarsening}$ , the boundary migration rate is larger than the coarsening rate and the precipitates detach from the boundary easily. Thus, the morphology of coarsened precipitates remains spherical in Fig. 12(a), as proved by Fig. 12(b). In the medium stage, the L1<sub>2</sub> phase coarsens into the lamellar shape due to the slowed migration rate and increased time for coarsening,  $v_{boundary} < v_{coarsening}$ , which makes the precipitates coarsen directionally along the moving direction of the grain boundary (Fig. 12(c)). The morphology is then formed with the inner-spherical and border lamellar precipitates in the RX area (Fig. 12(d)). In the last stage, the boundary migration rate decreases further with the decreased dislocation density in Fig. 12(e). The coarsening behavior of lamellar shape precipitates is more obvious because of the long-time boundary diffusion. The coarsened-lamellar precipitates with larger sizes are shown in Fig. 12(f). Controlled by above discontinuous coarsening behavior, heterogeneous precipitates with the inner spherical and boundary lamellar shapes are formed.

## 5. Conclusions

In summary, we investigated the mechanical behaviors and deformation mechanisms of precipitation-hardened HEAs with different recrystallization volume fractions by μ-DIC, TEM, and EBSD analysis. For the first time, we evidenced that the discontinuous coarsening generated heterogeneous precipitates keep the tensile properties of partially recrystallized HEAs unchanged. The main

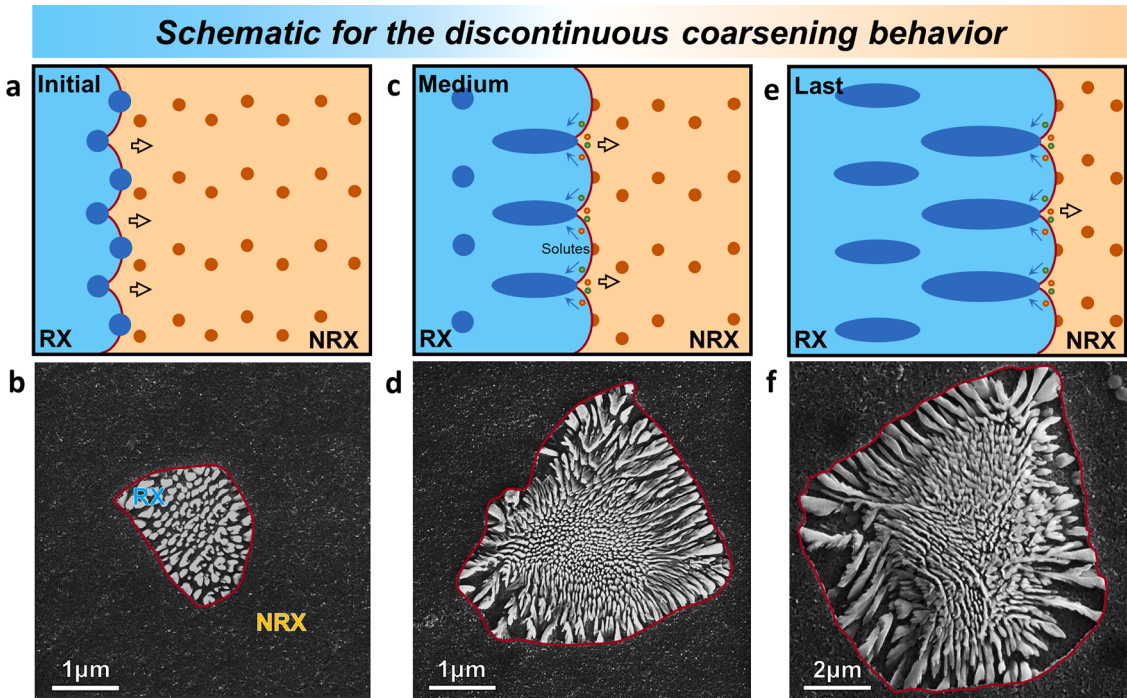


**Fig. 12.** Schematic of the microstructure evolution process of CHEAs during the discontinuous coarsening process, (a) initial stage of the discontinuous coarsening, (b) shows the experimental morphology of the initial concurrent recrystallization and precipitation, (c) medium stage of the discontinuous coarsening, (d) shows the lamellar precipitate after swept by the boundary, (e) last stage of the discontinuous coarsening, (f) shows the lamellar precipitates with larger size. The left blue area represents the RX region, the right yellow area represents the NRG region, and the red lines represent the moving boundary in (a-c). (For interpretation of the references to colour in this figure legend, the reader is referred to the web version of this article.)

conclusions are as follows:

- 1) The mechanical properties of the Ni<sub>2</sub>CoCrFeTi<sub>0.24</sub>Al<sub>0.2</sub> HEAs are almost the same with different recrystallization fractions of 21 %, 57 %, and 72 %, i.e., yield strength ~1.3 GPa, ultimate tensile strength ~1.5 GPa, and uniform elongation ~15 %. The unchanged yield strength comes from the increase of precipitate strengthening and boundary strengthening which equivalently compensates for the decrease in continuous precipitate strengthening and dislocation strengthening.
- 2) The origins of the unchanged ductility were revealed. Combining the variate-controlled LUR tensile and high-resolution μ-DIC experiments, we identified two HDI stress sources, i.e., hetero-deformation between RX and NRX areas and hetero-deformation between areas with lamellar and spherical precipitates. Based on a modified theoretical model, the inter-transformation between these two HDI stresses contributes to unchanged ductility
- 3) The discontinuous coarsening process is responsible for the formation of heterogeneous precipitates in Ni<sub>2</sub>CoCrFeTi<sub>0.24</sub>Al<sub>0.2</sub> during recrystallization. This typical discontinuous coarsening process is confirmed by an unchanged precipitate volume fraction (~30 %), a sharp transition in precipitate size (from ~10 nm to ~100 nm), and a discontinuous change in composition between the RX and NRX areas. During the discontinuous coarsening, precipitates coarsen through boundary-diffusion on the recrystallized grain boundaries and thus become larger than those in NRX regions. As the boundary further migrates, precipitates coarsen along the moving direction, resulting in heterogeneous precipitates with spherical shapes inside the grains and lamellar shapes near the grain boundaries.

#### CRediT authorship contribution statement

**Zhongsheng Yang:** Writing – original draft, Visualization, Methodology, Investigation, Funding acquisition, Formal analysis. **Xin Liu:** Validation, Investigation. **Jiajun Zhao:** Investigation, Data curation. **Qionghuan Zeng:** Investigation. **Kengfeng Xu:** Investigation. **Yue Li:** Investigation. **Chuanyun Wang:** Methodology. **Lei Wang:** Formal analysis. **Junjie Li:** Formal analysis. **Jincheng Wang:** Formal analysis. **Hyoung Seop Kim:** Writing – review & editing, Investigation. **Zhijun Wang:** Writing – review & editing, Supervision, Funding acquisition, Conceptualization. **Feng He:** Writing – review & editing, Supervision, Funding acquisition, Conceptualization.

#### Declaration of competing interest

The authors declare that they have no known competing financial interests or personal relationships that could have appeared to influence the work reported in this paper.

#### Data availability

Data will be made available on request.

#### Acknowledgment

The authors are grateful for the financial support by the National Natural Science Foundation of China (No. 52001266), the Guangdong Basic and Applied Basic Research Foundation (No. 2023A1515012703), the Shanghai “Phosphor” Science Foundation, China (23YF1450900), the Fundamental Research Funds for the Central Universities (No. G2022KY05109), the Research Fund of the State Key Laboratory of Solidification Processing (NPU), China (Grant No. 2023-QZ-02), the Innovation Foundation for Doctor Dissertation of Northwestern Polytechnical University (No. CX2023047) and Young Elite Scientists Sponsorship Program by CAST, Grant No. 2023QNRC001. Zhongsheng Yang sincerely thanks Dr. Qingfeng Wu, Bojing Guo and Dingcong Cui for the fruitful discussion on in-situ experiments and microstructure evolution. All authors sincerely acknowledge the reviewers for professional and valuable suggestions that have dramatically improved our manuscript.

#### Supplementary materials

Supplementary material associated with this article can be found, in the online version, at [doi:10.1016/j.ijplas.2024.103963](https://doi.org/10.1016/j.ijplas.2024.103963).

#### References

- An, F., Hou, J., Liu, J., Qian, B., Lu, W., 2023. Deformable κ phase induced deformation twins in a CoNiV medium entropy alloy. *Int. J. Plast.* 160, 103509 <https://doi.org/10.1016/j.ijplas.2022.103509>.
- Britton, B.T., Wilkinson, A.J., 2012. Stress fields and geometrically necessary dislocation density distributions near the head of a blocked slip band. *Acta Mater.* 60, 5773–5782. <https://doi.org/10.1016/j.actamat.2012.07.004>.
- Cao, Z.H., Zhai, G.Y., Ma, Y.J., Ding, L.P., Li, P.F., Liu, H.L., Lu, H.M., Cai, Y.P., Wang, G.J., Meng, X.K., 2021. Evolution of interfacial character and its influence on strain hardening in dual-phase high entropy alloys at nanoscale. *Int. J. Plast.* 145, 103081 <https://doi.org/10.1016/j.ijplas.2021.103081>.

- Chellman, D.J., Ardell, A.J., 1974. The coarsening of  $\gamma'$  precipitates at large volume fractions. *Acta Metall.* 22, 577–588. [https://doi.org/10.1016/0001-6160\(74\)90155-2](https://doi.org/10.1016/0001-6160(74)90155-2).
- Chou, T.H., Li, W.P., Chang, H.W., Du, X.H., Chuang, W.S., Yang, T., Zhu, Y.T., Huang, J.C., 2022. Quantitative analysis of hetero-deformation induced strengthening in heterogeneous grain structure. *Int. J. Plast.* 159 <https://doi.org/10.1016/j.ijplas.2022.103482>.
- Cui, D., Yuyu, Z., Liu, L., Zhijun, W., 2023. Oxygen-assisted spinodal structure achieves 1.5 GPa yield strength in a ductile refractory high-entropy alloy. *J. Mater. Sci. Technol.* 157, 11–20. <https://doi.org/10.1016/j.jmst.2023.01.038>.
- Dasari, S., Chang, Y.J., Jagetia, A., Soni, V., Sharma, A., Gwalani, B., Gorsse, S., Yeh, A.C., Banerjee, R., 2021. Discontinuous precipitation leading to nano-rod intermetallic precipitates in an Al0.2Ti0.3Co1.5CrFeNi1.5 high entropy alloy results in an excellent strength-ductility combination. *Mater. Sci. Eng. A* 805, 140551. <https://doi.org/10.1016/j.msea.2020.140551>.
- Du, X.H., Li, W.P., Chang, H.T., Yang, T., Duan, G.S., Wu, B.L., Huang, J.C., Chen, F.R., Liu, C.T., Chuang, W.S., Lu, Y., Sui, M.L., Huang, E.W., 2020. Dual heterogeneous structures lead to ultrahigh strength and uniform ductility in a Co-Cr-Ni medium-entropy alloy. *Nat. Commun.* 11, 1–7. <https://doi.org/10.1038/s41467-020-16085-z>.
- Fan, J., Ji, X., Fu, L., Wang, J., Ma, S., Sun, Y., Wen, M., Shan, A., 2022. Achieving exceptional strength-ductility synergy in a complex-concentrated alloy via architected heterogeneous grains and nano-sized precipitates. *Int. J. Plast.* 157, 103398 <https://doi.org/10.1016/j.ijplas.2022.103398>.
- Fan, L., Yang, T., Zhao, Y., Luan, J., Zhou, G., Wang, H., Jiao, Z., Liu, C.T., 2020. Ultrahigh strength and ductility in newly developed materials with coherent nanolamellar architectures. *Nat. Commun.* 11, 1–8. <https://doi.org/10.1038/s41467-020-20109-z>.
- Fang, J.Y.C., Liu, W.H., Luan, J.H., Yang, T., Fu, M.W., Jiao, Z.B., 2022a. Dual effects of pre-strain on continuous and discontinuous precipitation of L12-strengthened high-entropy alloys. *J. Alloys Compd.* 925 <https://doi.org/10.1016/j.jallcom.2022.166730>.
- Fang, J.Y.C., Liu, W.H., Luan, J.H., Yang, T., Wu, Y., Fu, M.W., Jiao, Z.B., 2022b. Competition between continuous and discontinuous precipitation in L12-strengthened high-entropy alloys. *Intermetallics* 149. <https://doi.org/10.1016/j.intermet.2022.107655>.
- Fang, Q., Chen, Y., Li, J., Jiang, C., Liu, B., Liu, Y., Liaw, P.K., 2019. Probing the phase transformation and dislocation evolution in dual-phase high-entropy alloys. *Int. J. Plast.* 114, 161–173. <https://doi.org/10.1016/j.ijplas.2018.10.014>.
- Fu, W., Huang, Y., Sun, J., Ngan, A.H.W., 2022. Strengthening CrFeCoNiMn0.75Cu0.25 high entropy alloy via laser shock peening. *Int. J. Plast.* 154, 103296 <https://doi.org/10.1016/j.ijplas.2022.103296>.
- George, E.P., Curtin, W.A., Tasan, C.C., 2020. High entropy alloys: a focused review of mechanical properties and deformation mechanisms. *Acta Mater.* 188, 435–474. <https://doi.org/10.1016/j.actamat.2019.12.015>.
- Guo, F.J., Wang, Y.F., Wang, M.S., Wei, W., He, Q., Wang, Q.Y., Jin, R.R., Huang, C.X., 2022. The critical grain size for optimal strength-ductility synergy in CrCoNi medium entropy alloy. *Scr. Mater.* 218, 29–33. <https://doi.org/10.1016/j.scriptamat.2022.114808>.
- Guo, Y., Collins, D.M., Tarleton, E., Hofmann, F., Wilkinson, A.J., Britton, T.Ben, 2020. Dislocation density distribution at slip band-grain boundary intersections. *Acta Mater.* 182, 172–183. <https://doi.org/10.1016/j.actamat.2019.10.031>.
- Gwalani, B., Dasari, S., Sharma, A., Soni, V., Shukla, S., Jagetia, A., Agrawal, P., Mishra, R.S., Banerjee, R., 2021. High density of strong yet deformable intermetallic nanorods leads to an excellent room temperature strength-ductility combination in a high entropy alloy. *Acta Mater.* 219 <https://doi.org/10.1016/j.actamat.2021.117234>.
- Hasan, M.N., Liu, Y.F., An, X.H., Gu, J., Song, M., Cao, Y., Li, Y.S., Zhu, Y.T., Liao, X.Z., 2019. Simultaneously enhancing strength and ductility of a high-entropy alloy via gradient hierarchical microstructures. *Int. J. Plast.* 123, 178–195. <https://doi.org/10.1016/j.ijplas.2019.07.017>.
- He, F., Wei, S., Cann, J.L., Wang, Z., Wang, J., Tasan, C.C., 2021a. Composition-dependent slip planarity in mechanically-stable face centered cubic complex concentrated alloys and its mechanical effects. *Acta Mater.* 220, 117314 <https://doi.org/10.1016/j.actamat.2021.117314>.
- He, F., Yang, Z., Liu, S., Chen, D., Lin, W., Yang, T., Wei, D., Wang, Z., Wang, J., Kai, J.Jung, 2021b. Strain partitioning enables excellent tensile ductility in precipitated heterogeneous high-entropy alloys with gigapascal yield strength. *Int. J. Plast.* 144 <https://doi.org/10.1016/j.ijplas.2021.103022>.
- He, Z., Jia, N., Yan, H., Shen, Y., Zhu, M., Guan, X., Zhao, X., Jin, S., Sha, G., Zhu, Y., Liu, C.T., 2021. Multi-heterostructure and mechanical properties of N-doped FeMnCoCr high entropy alloy. *Int. J. Plast.* 139, 102965 <https://doi.org/10.1016/j.ijplas.2021.102965>.
- Huang, C.X., Wang, Y.F., Ma, X.L., Yin, S., Höppel, H.W., Göken, M., Wu, X.L., Gao, H.J., Zhu, Y.T., 2018. Interface affected zone for optimal strength and ductility in heterogeneous laminate. *Mater. Today* 21, 713–719. <https://doi.org/10.1016/j.mattod.2018.03.006>.
- Humphreys, J., Rohrer, G.S., Rollett, A., 2017. Chapter 7 - Recrystallization of Single-Phase Alloys, Third Ed. Elsevier, Oxford, pp. 245–304. <https://doi.org/10.1016/B978-0-08-098235-9.00007-0>.
- Jo, Y.H., Jung, S., Choi, W.M., Sohn, S.S., Kim, H.S., Lee, B.J., Kim, N.J., Lee, S., 2017. Cryogenic strength improvement by utilizing room-temperature deformation twinning in a partially recrystallized VCrMnFeCoNi high-entropy alloy. *Nat. Commun.* 8, 1–8. <https://doi.org/10.1038/ncomms15719>.
- Kaushik, L., Kim, M.S., Singh, J., Kang, J.H., Heo, Y.U., Suh, J.Y., Choi, S.H., 2021. Deformation mechanisms and texture evolution in high entropy alloy during cold rolling. *Int. J. Plast.* 141, 102989 <https://doi.org/10.1016/j.ijplas.2021.102989>.
- Li, J., Chen, S., Weng, G.J., Lu, W., 2021a. A micromechanical model for heterogeneous nanograined metals with shape effect of inclusions and geometrically necessary dislocation pileups at the domain boundary. *Int. J. Plast.* 144, 103024 <https://doi.org/10.1016/j.ijplas.2021.103024>.
- Li, J., Soh, A.K., 2012. Modeling of the plastic deformation of nanostructured materials with grain size gradient. *Int. J. Plast.* 39, 88–102. <https://doi.org/10.1016/j.ijplas.2012.06.004>.
- Li, J., Weng, G.J., Chen, S., Wu, X., 2017. On strain hardening mechanism in gradient nanostructures. *Int. J. Plast.* 88, 89–107. <https://doi.org/10.1016/j.ijplas.2016.10.003>.
- Li, W., Chou, T.H., Yang, T., Chuang, W.S., Huang, J.C., Luan, J., Zhang, X., Huo, X., Kong, H., He, Q., Du, X., Liu, C.T., Chen, F.R., 2021b. Design of ultrastrong but ductile medium-entropy alloy with controlled precipitations and heterogeneous grain structures. *Appl. Mater. Today* 23. <https://doi.org/10.1016/j.apmt.2021.101037>.
- Li, Y., Zhang, H., Shang, X., Liu, M., Zhao, S., Cui, Z., 2022. A multiscale investigation on the preferential deformation mechanism of coarse grains in the mixed-grain structure of 316LN steel. *Int. J. Plast.* 152, 103244 <https://doi.org/10.1016/j.ijplas.2022.103244>.
- Li, Y.X., Nutor, R.K., Zhao, Q.K., Zhang, X.P., Cao, Q.P., Sohn, S.S., Wang, X.D., Ding, S.Q., Zhang, D.X., Zhou, H.F., Wang, J.W., Jiang, J.Z., 2023. Unraveling the deformation behavior of the Fe45Co25Ni10V20 high entropy alloy. *Int. J. Plast.* 165, 103619 <https://doi.org/10.1016/j.ijplas.2023.103619>.
- Liu, L., Zhang, Y., Zhang, Z., Li, J., Jiang, W., Sun, L., 2024. Nanoprecipitate and stacking fault-induced high strength and ductility in a multiscale heterostructured high-entropy alloy. *Int. J. Plast.* 172, 103853 <https://doi.org/10.1016/j.ijplas.2023.103853>.
- Liu, X., Jiang, S., Lu, J., Wei, J., Wei, D., He, F., 2022. The dual effect of grain size on the strain hardening behaviors of Ni-Co-Cr-Fe high entropy alloys. *J. Mater. Sci. Technol.* <https://doi.org/10.1016/j.jmst.2022.06.001>.
- Liu, Yanfang, Cao, Y., Mao, Q., Zhou, H., Zhao, Y., Jiang, W., Liu, Ying, Wang, J.T., You, Z., Zhu, Y., 2020. Critical microstructures and defects in heterostructured materials and their effects on mechanical properties. *Acta Mater.* 189, 129–144. <https://doi.org/10.1016/j.actamat.2020.03.001>.
- Luo, Z., Li, J., Feng, T., Lu, K., Ma, X., 2023. Optimizing heterostructure parameters for enhanced mechanical performance of Al0.1CoCrFeNi high entropy alloy. *Mater. Sci. Eng. A* 885, 145623. <https://doi.org/10.1016/j.msea.2023.145623>.
- Ma, E., Wu, X., 2019. Tailoring heterogeneities in high-entropy alloys to promote strength-ductility synergy. *Nat. Commun.* 10, 1–10. <https://doi.org/10.1038/s41467-019-13311-1>.
- Manna, I., Pabi, S.K., Gust, W., 2001. Discontinuous reactions in solids. *Int. Mater. Rev.* 46, 53–91. <https://doi.org/10.1179/095066001101528402>.
- Ming, K., Bi, X., Wang, J., 2019. Strength and ductility of CrFeCoNiMo alloy with hierarchical microstructures. *Int. J. Plast.* 113, 255–268. <https://doi.org/10.1016/j.ijplas.2018.10.005>.
- Ming, K., Bi, X., Wang, J., 2018. Realizing strength-ductility combination of coarse-grained Al0.2Co1.5CrFeNi1.5Ti0.3 alloy via nano-sized, coherent precipitates. *Int. J. Plast.* 100, 177–191. <https://doi.org/10.1016/j.ijplas.2017.10.005>.
- Nie, J., Chen, Y., Song, L., Fan, Y., Cao, Y., Xie, K., Liu, S., Liu, X., Zhao, Y., Zhu, Y., 2023. Enhancing strength and ductility of Al-matrix composite via a dual-heterostructure strategy. *Int. J. Plast.* 171, 103825 <https://doi.org/10.1016/j.ijplas.2023.103825>.

- Park, H.K., Ameyama, K., Yoo, J., Hwang, H., Kim, H.S., 2018. Additional hardening in harmonic structured materials by strain partitioning and back stress. *Mater. Res. Lett.* 6, 261–267. <https://doi.org/10.1080/21663831.2018.1439115>.
- Sathiyamoorthi, P., Kim, H.S., 2022. High-entropy alloys with heterogeneous microstructure: processing and mechanical properties. *Prog. Mater. Sci.* 123, 100709 <https://doi.org/10.1016/j.pmatsci.2020.100709>.
- Schneider, M., George, E.P., Manescu, T.J., Záležák, T., Hunfeld, J., Dlouhý, A., Eggeler, G., Laplanche, G., 2020. Analysis of strengthening due to grain boundaries and annealing twin boundaries in the CrCoNi medium-entropy alloy. *Int. J. Plast.* 124, 155–169. <https://doi.org/10.1016/j.ijplas.2019.08.009>.
- Shen, J., Lopes, J.G., Zeng, Z., Choi, Y.T., Maawad, E., Schell, N., Kim, H.S., Mishra, R.S., Oliveira, J.P., 2023. Deformation behavior and strengthening effects of an eutectic AlCoCrFeNi2.1 high entropy alloy probed by in-situ synchrotron X-ray diffraction and post-mortem EBSD. *Mater. Sci. Eng. A* 872, 144946. <https://doi.org/10.1016/j.msea.2023.144946>.
- Shen, J., Zhang, W., Lopes, J.G., Pei, Y., Zeng, Z., Maawad, E., Schell, N., Baptista, A.C., Mishra, R.S., Oliveira, J.P., 2024. Evolution of microstructure and deformation mechanisms in a metastable Fe42Mn28Co10Cr15Si5 high entropy alloy: a combined in-situ synchrotron X-ray diffraction and EBSD analysis. *Mater. Des.* 238, 112662 <https://doi.org/10.1016/j.matdes.2024.112662>.
- Shukla, S., Choudhuri, D., Wang, T., Liu, K., Wheeler, R., Williams, S., Gwalani, B., Mishra, R.S., 2018. Hierarchical features infused heterogeneous grain structure for extraordinary strength-ductility synergy. *Mater. Res. Lett.* 6, 676–682. <https://doi.org/10.1080/21663831.2018.1538023>.
- Salone, C.E., Miao, J., George, E.P., Mills, M.J., 2019. Achieving ultra-high strength and ductility in equiatomic CrCoNi with partially recrystallized microstructures. *Acta Mater.* 165, 496–507. <https://doi.org/10.1016/j.actamat.2018.12.015>.
- Wagner, C., Laplanche, G., 2023. Effect of grain size on critical twinning stress and work hardening behavior in the equiatomic CrMnFeCoNi high-entropy alloy. *Int. J. Plast.* 166, 103651 <https://doi.org/10.1016/j.ijplas.2023.103651>.
- Wang, R., Tang, Y., Ai, Y., Li, S., Zhu, L., Bai, S., 2024. Strengthening and ductilization of a refractory high-entropy alloy over a wide strain rate range by multiple heterostructures. *Int. J. Plast.* 173, 103882 <https://doi.org/10.1016/j.ijplas.2024.103882>.
- Wang, Y., Huang, C., Li, Y., Guo, F., He, Q., Wang, M., Wu, X., Scattergood, R.O., Zhu, Y., 2020. Dense dispersed shear bands in gradient-structured Ni. *Int. J. Plast.* 124, 186–198. <https://doi.org/10.1016/j.ijplas.2019.08.012>.
- Wang, Y., Huang, C., Ma, X., Zhao, J., Guo, F., Fang, X., Zhu, Y., Wei, Y., 2023. The optimum grain size for strength-ductility combination in metals. *Int. J. Plast.* 164, 103574 <https://doi.org/10.1016/j.ijplas.2023.103574>.
- Wang, Y., Wei, Y., Zhao, Z., Long, H., Lin, Z., Guo, F., He, Q., Huang, C., Zhu, Y., 2022a. Activating dispersed strain bands in tensioned nanostructure layer for high ductility: the effects of microstructure inhomogeneity. *Int. J. Plast.* 149, 103159 <https://doi.org/10.1016/j.ijplas.2021.103159>.
- Wang, Y., Zhu, Y., Yu, Z., Zhao, J., Wei, Y., 2022b. Hetero-zone boundary affected region: a primary microstructural factor controlling extra work hardening in heterostructure. *Acta Mater.* 241, 118395 <https://doi.org/10.1016/j.actamat.2022.118395>.
- Wang, Y.F., Wang, M.S., Fang, X.T., Guo, F.J., Liu, H.Q., Scattergood, R.O., Huang, C.X., Zhu, Y.T., 2019. Extra strengthening in a coarse/ultrafine grained laminate: role of gradient interfaces. *Int. J. Plast.* 123, 196–207. <https://doi.org/10.1016/j.ijplas.2019.07.019>.
- Wei, D., Gong, W., Tsuru, T., Kawasaki, T., Harjo, S., Cai, B., Liaw, P.K., Kato, H., 2022a. Mechanical behaviors of equiatomic and near-equiatomic face-centered-cubic phase high-entropy alloys probed using in situ neutron diffraction. *Int. J. Plast.* 158, 103417 <https://doi.org/10.1016/j.ijplas.2022.103417>.
- Wei, D., Gong, W., Tsuru, T., Lobzenko, I., Li, X., Harjo, S., Kawasaki, T., Do, H.S., Bae, J.W., Wagner, C., Laplanche, G., Koizumi, Y., Adachi, H., Aoyagi, K., Chiba, A., Lee, B.J., Kim, H.S., Kato, H., 2022b. Si-addition contributes to overcoming the strength-ductility trade-off in high-entropy alloys. *Int. J. Plast.* 159, 103443 <https://doi.org/10.1016/j.ijplas.2022.103443>.
- Wei, S., Kim, J., Tasan, C.C., 2022. In-situ investigation of plasticity in a Ti-Al-V-Fe ( $\alpha+\beta$ ) alloy: slip mechanisms, strain localization, and partitioning. *Int. J. Plast.* 148, 103131 <https://doi.org/10.1016/j.ijplas.2021.103131>.
- Wei, S., Kim, S.J., Kang, J., Zhang, Yong, Zhang, Yongjie, Furuhara, T., Park, E.S., Tasan, C.C., 2020. Natural-mixing guided design of refractory high-entropy alloys with as-cast tensile ductility. *Nat. Mater.* 19, 1175–1181. <https://doi.org/10.1038/s41563-020-0750-4>.
- Wu, H., Huang, M., Xia, Y., Li, X., Li, R., Liu, C., Gan, W., Xiao, T., Geng, L., Liu, Q., Fan, G., 2023. The importance of interfacial stress-affected zone in evading the strength-ductility trade-off of heterogeneous multi-layered composites. *Int. J. Plast.* 160, 103485 <https://doi.org/10.1016/j.ijplas.2022.103485>.
- Wu, Q., He, F., Li, J., Kim, H.S., Wang, Z., Wang, J., 2022. Phase-selective recrystallization makes eutectic high-entropy alloys ultra-ductile. *Nat. Commun.* 13 <https://doi.org/10.1038/s41467-022-32444-4>.
- Wu, S.W., Wang, G., Jia, Y.D., Yi, J., Zhai, Q.J., Liu, C.T., Sun, B.A., Chu, H.J., Shen, J., Liaw, P.K., Zhang, T.Y., 2019a. Enhancement of strength-ductility trade-off in a high-entropy alloy through a heterogeneous structure. *Acta Mater.* 165, 444–458. <https://doi.org/10.1016/j.actamat.2018.12.012>.
- Wu, S.W., Wang, G., Jia, Y.D., Yi, J., Zhai, Q.J., Liu, C.T., Sun, B.A., Chu, H.J., Shen, J., Liaw, P.K., Zhang, T.Y., 2019b. Enhancement of strength-ductility trade-off in a high-entropy alloy through a heterogeneous structure. *Acta Mater.* 165, 444–458. <https://doi.org/10.1016/j.actamat.2018.12.012>.
- Wu, X., Yang, M., Yuan, F., Wu, G., Wei, Y., Huang, X., Zhu, Y., 2015. Heterogeneous lamella structure unites ultrafine-grain strength with coarse-grain ductility. *Proc. Natl. Acad. Sci. USA* 112, 14501–14505. <https://doi.org/10.1073/pnas.1517193112>.
- Xu, W.W., Xiong, Z.Y., Li, Z.N., Gao, X., Li, W., Yang, T., Li, X.Q., Vitos, L., Liu, C.T., 2022. Atomic origins of the plastic deformation micro-mechanisms of  $\gamma/\gamma'$  FeCoNiAlTi high-entropy alloys. *Int. J. Plast.* 158, 103439 <https://doi.org/10.1016/j.ijplas.2022.103439>.
- Yang, G., Kim, J.K., 2022. Hierarchical precipitates, sequential deformation-induced phase transformation, and enhanced back stress strengthening of the micro-alloyed high entropy alloy. *Acta Mater.* 233, 117974 <https://doi.org/10.1016/j.actamat.2022.117974>.
- Yang, M., Pan, Y., Yuan, F., Zhu, Y., Wu, X., 2016. Back stress strengthening and strain hardening in gradient structure. *Mater. Res. Lett.* 4, 145–151. <https://doi.org/10.1080/21663831.2016.1153004>.
- Yang, M., Yan, D., Yuan, F., Jiang, P., Ma, E., Wu, X., 2018. Dynamically reinforced heterogeneous grain structure prolongs ductility in a medium-entropy alloy with gigapascal yield strength. *Proc. Natl. Acad. Sci. USA* 115, 7224–7229. <https://doi.org/10.1073/pnas.1807817115>.
- Yang, Z., He, F., Wu, Q., Zhang, K., Cui, D., Guo, B., Han, B., Li, J., Wang, J., Wang, Z., 2021. Distinct recrystallization kinetics in Ni-Co-Cr-Fe-based single-phase high-entropy alloys. *Metall. Mater. Trans. A Phys. Metall. Mater. Sci.* 52, 3799–3810. <https://doi.org/10.1007/s11661-021-06341-2>.
- Yang, Z., Wang, Z., Guo, B., Cao, R., Wu, Q., Cui, D., Zhang, K., Li, J., Wang, J., He, F., 2022. Non-monotonic effect of pre-strain on the precipitates and strengthening mechanisms of high-entropy alloys. *J. Alloys Compd.* 906, 164338 <https://doi.org/10.1016/j.jallcom.2022.164338>.
- Yeh, J.W., Chen, S.K., Lin, S.J., Gan, J.Y., Chin, T.S., Shun, T.T., Tsau, C.H., Chang, S.Y., 2004. Nanostructured high-entropy alloys with multiple principal elements: novel alloy design concepts and outcomes. *Adv. Eng. Mater.* 6, 299–303. <https://doi.org/10.1002/adem.200300567>.
- Yu, L., Luo, H., 2019. Effect of partial recrystallization annealing on magnetic properties and mechanical properties of non-oriented silicon steel. *Acta Met. Sin* 56, 291–300.
- Zhang, X., Gui, Y., Lai, M., Lu, X., Gu, J., Wang, F., Yang, T., Wang, Z., Song, M., 2023a. Enhanced strength-ductility synergy of medium-entropy alloys via multiple level gradient structures. *Int. J. Plast.* 164, 103592 <https://doi.org/10.1016/j.ijplas.2023.103592>.
- Zhang, X., Zhao, J., Kang, G., Zaiser, M., 2023b. Geometrically necessary dislocations and related kinematic hardening in gradient grained materials: a nonlocal crystal plasticity study. *Int. J. Plast.* 163, 103553 <https://doi.org/10.1016/j.ijplas.2023.103553>.
- Zhang, Z., Ma, Y., Yang, M., Jiang, P., Feng, H., Zhu, Y., Wu, X., Yuan, F., 2024. Improving ductility by coherent nanoprecipitates in medium entropy alloy. *Int. J. Plast.* 172, 103821 <https://doi.org/10.1016/j.ijplas.2023.103821>.
- Zhao, J., Zaiser, M., Lu, X., Zhang, B., Huang, C., Kang, G., Zhang, X., 2021. Size-dependent plasticity of hetero-structured laminates: a constitutive model considering deformation heterogeneities. *Int. J. Plast.* 145, 103063 <https://doi.org/10.1016/j.ijplas.2021.103063>.
- Zhang, C.L., Bao, X.Y., Zhang, D.D., Chen, W., Zhang, J.Y., Kuang, J., Liu, G., Sun, J., 2021. Achieving superior strength-ductility balance in a novel heterostructured strong metastable  $\beta$ -Ti alloy. *Int. J. Plast.* 147, 103126 <https://doi.org/10.1016/j.ijplas.2021.103126>.